# Eye Formation and Energetics in a Dry Model of Hurricane-Like Vortices

EMMANUEL DORMY,[a] LUDIVINE ORUBA,[b] AND KERRY EMANUEL[c]

[a] *Département de Mathématiques et Applications, UMR-8553, École Normale Supérieure, CNRS, PSL University, Paris, France*
[b] *Laboratoire Atmosphères, Observations Spatiales, Sorbonne Université, UVSQ, CNRS, Paris, France*
[c] *Lorenz Center, Massachusetts Institute of Technology, Cambridge, Massachusetts*

(Manuscript received 20 October 2023, in final form 30 April 2024, accepted 2 June 2024)

ABSTRACT: We investigate the mechanism for eye formation in hurricane-like vortices, using a formulation adapted from Oruba, Davidson, and Dormy. Numerical simulations are performed using an axisymmetric model of dry rotating Rayleigh–Bénard convection under the Boussinesq approximation. The fluxes of heat and momentum at the sea surface are described using the bulk aerodynamic formula. A simplified model for radiative cooling is also implemented. We find that the mechanism for eye formation introduced in Oruba et al., relying on vorticity stripping from the boundary layer, is robust in dry hurricane-like vortices. Furthermore, with these boundary conditions, the structure of the flow is closer to the flow of actual tropical cyclones. The applicability of this mechanism to the moist case however remains uncertain and deserves further study. Finally, energy budgets, obtained either by a heat engine approach or by a direct estimation of the work of buoyancy forces, are investigated. They provide estimations of the surface wind speed as a function of the controlling parameters.

SIGNIFICANCE STATEMENT: Tropical cyclones (also known as hurricanes or typhoons, depending on their location) are life-threatening and devastating atmospheric vortices. Their impact worsens with sea level rise and increasing coastal population. Here, we explore, using idealized models, the physics behind the formation of an eye (the quiet and typically clear region at the center of these storms). We then investigate the controlling parameters for the amplitude of the strongest winds in the model, using energy constraints, and compare them to what is observed in actual tropical cyclones.

KEYWORDS: Hurricanes/typhoons; Tropical cyclones; Thermodynamics; Boundary conditions; Idealized models

## 1. Introduction

The eye is probably the most emblematic feature of tropical cyclones (TCs), yet the underlying mechanisms responsible for the eye formation remain an open issue (e.g., Pearce 2005a; Smith 2005; Pearce 2005b). The eye corresponds to the central region characterized by relatively calm winds, diminished precipitation, and subsiding air. Several theories aim at explaining eye subsidence, which is a key feature of the eye in TCs. The causes for eye subsidence include dynamically forced subsidence, convectively forced driven subsidence, and forcing due to local perturbation pressure gradient force. The historic "centrifugal" hypothesis, first described by Ballou (1892) and further elaborated by Malkus (1958) and Kuo (1959), relies on the idea that the eye air mixes with the high angular momentum eyewall air which becomes supergradient. This causes it to be centrifuged out of the eye at low level, resulting in eye subsidence through mass conservation. In a second theory, based on Eliassen's 1952 balanced vortex theory, Willoughby (1979) and Shapiro and Willoughby (1982) described the eye subsidence as forced by radial gradients of convective heating associated with the latent heat release in the eyewall. An alternative view was proposed by Smith (1980), in which the eye subsidence is forced by a reduced pressure gradient force, compared to the environment which is in hydrostatic balance, resulting from the decrease in the radial pressure gradient with altitude. In addition to these theories, Pearce (1998) tackled the eye formation problem using a two-layer model; he identified gravity waves, vortex tilting, and azimuthal vorticity production as key ingredients in eye formation, but his conclusions are still under debate. For a detailed review on the formation of hurricane eye, the reader is referred to Vigh (2010).

TCs develop in a complex environment involving stratification, latent heat release, microphysics, and small-scale turbulence. Yet the eye is a ubiquitous and robust feature, suggesting that the underlying mechanisms may be at least partially independent of these complexities. To put the idea of a simple hydrodynamic mechanism to the test, Oruba et al. (2017, 2018) started by considering what is perhaps the simplest system in which eyes may form, namely, steady axisymmetric Boussinesq convection in a rotating cylindrical setup, with classical boundary conditions. The effects of stratification and of moist convection were neglected. It was observed that, in this configuration, for sufficiently vigorous flows, an eye can form. The key role played by the bottom boundary layer in providing the source of negative azimuthal vorticity for the eyewall was highlighted. In this setup, the vortex tilting term does not produce any net vorticity. It was shown that the negative vorticity in the bottom boundary layer is advected to the eyewall and that an eye then forms via cross-stream diffusion. Using the same model, but increasing the forcing, Atkinson et al. (2019) showed that the eye oscillates and highlighted the presence of trapped inertial waves at the center of the vortex.

*Corresponding author*: Emmanuel Dormy, emmanuel.dormy@ens.fr

DOI: 10.1175/JAS-D-23-0191.1

The use of idealized models to better understand the processes at stake in TCs is a natural approach, which is complementary to studies performed using more advanced models or observations (Emanuel 2020). Modeling TCs as isolated structures in idealized configurations has proven successful to identify key mechanisms in several previous investigations (e.g., Rotunno and Emanuel 1987; Bryan and Rotunno 2009; Tang and Emanuel 2012). Among these simplified models, numerical simulations in a dry atmosphere have already proven successful for the development of hurricane-like vortices, in two dimensions (Mrowiec et al. 2011; Wang and Lin 2020) and in three dimensions (Cronin and Chavas 2019; Velez-Pardo and Cronin 2023). These studies challenge the idea that moisture is essential to model some aspects of tropical cyclones.

The important role played by the bottom boundary layer in the development of tropical cyclones has been much emphasized in the literature (e.g., Smith and Montgomery 2010). It is characterized by complex processes such as drag effects and turbulent diffusion occurring at the interface between the ocean and the atmosphere, where sensible heat, latent heat, and momentum are exchanged. The accuracy of atmospheric models highly depends on the parameterization of these fluxes. The parameterization derived by Monin and Obukhov's bulk formula (Monin and Obukhov 1954) is now widely used to describe the atmospheric boundary layer (Foken 2006). The bulk formula provides an idealized description of the fluxes at the sea surface without the need to fully resolve the small-scale eddies near the surface.

The role of radiative cooling in the intensification of tropical cyclones has also been highlighted in many studies. More precisely, the contrast between the clear-sky longwave radiative cooling and the longwave radiation absorbing clouded area creates a differential heating important for the cyclogenesis stage, as highlighted by Wing et al. (2016) and Muller and Romps (2018) using idealized moist convection numerical simulations. Although the longwave cloud-radiative forcing helps early intensification of a TC, it was not observed to increase the maximum winds (see Dai et al. 2023).

The boundary conditions used in the original model of Oruba et al. (2017, 2018) were applicable to a fluid dynamics experiment rather than an atmospheric flow. In this paper, the original model (denoted as ODD) is extended to incorporate more realistic conditions. The two ingredients successively tested in the model are the bulk flux formulation at the bottom boundary and the radiative cooling. The resulting models are described in section 2. Section 3 investigates the eye formation in these more realistic models. Scaling laws based on physical considerations are then presented in section 4 and successfully compared to earlier results on tropical cyclones. Our results are then discussed in section 5.

## 2. Models and governing equations

We consider the steady flow of a Boussinesq fluid in a rotating, cylindrical domain of height $H$ and radius $R$, with the aspect ratio $\varepsilon = H/R = 0.1$. The flow is described in the rotating frame, using cylindrical polar coordinates $(r, \phi, z)$. We further restrict ourselves to axisymmetric motions, so that we may decompose the velocity field into poloidal and azimuthal velocity components $\mathbf{u}_p = (u_r, 0, u_z)$ and $\mathbf{u}_\phi = (0, u_\phi, 0)$, which are both solenoidal.

### a. The ODD model

Our approach is based on the ODD model (Oruba et al. 2017, 2018), which we briefly summarize here. The static temperature profile is set to be $T_0^\star(z^\star) = \beta(H - z^\star)$, where the star superscript designates dimensional quantities. The motion is driven by buoyancy associated with the difference in temperature $\Delta T_0^\star = \beta H$ between the bounding surfaces $z^\star = 0$ and $z^\star = H$, which mimic the oceanic surface ($z^\star = 0$) and the tropopause ($z^\star = H$). In the following equations, all quantities are dimensionless; the length has been scaled with the height $H$ of the troposphere, the time with $\Omega^{-1}$, and the temperature with $\beta H$. The nondimensional equations governing the flow in the rotating frame are

$$\frac{D\mathbf{u}}{Dt} = -\nabla\pi - 2\mathbf{e}_z \times \mathbf{u} + \mathrm{Ek}\nabla^2\mathbf{u} + \mathrm{RaEk}^2\mathrm{Pr}^{-1}T\mathbf{e}_z, \tag{1a}$$

$$\nabla \cdot \mathbf{u} = 0, \quad \text{and} \tag{1b}$$

$$\frac{DT}{Dt} = \mathrm{EkPr}^{-1}\nabla^2 T, \tag{1c}$$

where $\mathbf{u}$ is the solenoidal velocity field in the rotating frame, $\pi$ is the departure from a hydrostatic pressure distribution, and $\mathbf{e}_z$ denotes a unit vector in the vertical direction. The dimensionless control parameters of the system are then the Ekman number $\mathrm{Ek} = \nu_t/\Omega H^2$, the Prandtl number $\mathrm{Pr} = \nu_t/\kappa_t$, and the Rayleigh number $\mathrm{Ra} = \alpha g \beta H^4/\nu_t\kappa_t$, where $g$ denotes the strength of gravity, $\kappa_t$ denotes the thermal eddy diffusivity of the air, $\alpha$ denotes its thermal expansion coefficient, and $\nu_t$ denotes the eddy viscosity of the flow. Due to the Boussinesq approximation, the potential temperature, which stems from the compressible nature of the air, is simply modeled here by the temperature $T$. The upward heat flux at the lower surface and at the top surface is assumed to be uniform and constant $\partial T/\partial z = -1$, and the heat flux through the outer boundary is assumed to vanish. The surfaces at $z^\star = 0$ and $r^\star = R$ are no-slip boundaries, while the upper surface is taken to be stress free. For details regarding the linear stability and nonlinear development in this penny-shaped geometry, we refer the reader to Soward et al. (2022). The large-scale mode investigated here is not the first amplified mode at onset, but it is nonlinearly realized.

### b. The $DOE_1$ model

In the first modified model investigated here, denoted as $\mathrm{DOE}_1$, the bottom boundary conditions have been modified for a more realistic description of the boundary layer. Instead of fixing the heat flux at the lower boundary and considering it as no slip, we introduce bulk aerodynamic formulae. In this approach, the surface sensible heat flux $F_h^\star$ (W m$^{-2}$) is related to the difference in temperature between the air at the surface $T^\star$ and the sea surface temperature $T_s^\star$, through the relation:

$$F_h^\star = -k_a\left(\frac{\partial T^\star}{\partial z^\star}\right)_{z^\star=0} = -\rho_a c_p C_H \sqrt{u_h^{\star 2} + U_g^{\star 2}}(T^\star - T_s^\star), \tag{2}$$

where $k_a$, $\rho_a$, and $c_p$ correspond to the thermal conductivity, the volumetric mass density, and the constant pressure specific heat of the atmosphere, respectively. The dimensionless heat exchange coefficient is denoted as $C_H$. In this description, the horizontal velocity at $z = 0$ is split into its numerically resolved part $u_h^\star = \sqrt{u_r^{\star 2} + u_\phi^{\star 2}}$, where $u_r^\star$ and $u_\phi^\star$ are the dimensional radial and azimuthal velocities, and its subgrid part quantified by the so-called gustiness wind $U_g^\star$ (e.g., Godfrey and Beljaars 1991). We introduce the nondimensional parameters:

$$\alpha_T = \frac{\rho_a c_p C_H H U_g^\star}{k_a}, \quad \beta_T = \left(\frac{\Omega H}{U_g^\star}\right)^2, \tag{3}$$

where $\beta_T$ corresponds to the square of an inverse Rossby number based on $U_g^\star$. Using the height $H$ as length scale, $\Omega^{-1}$ as time scale, and $\alpha_T T_s^\star$ as temperature scale yields

$$\left(\frac{\partial T}{\partial z}\right)_{z=0} = (-1 + \alpha_T T)\sqrt{1 + \beta_T u_h^2}. \tag{4}$$

The thus-obtained relation is the bottom boundary condition for the temperature field in our new model. In this model, the heat flux at the upper surface is maintained to $\partial T/\partial z = -1$, and the temperature at the external edge is fixed to $T = -z$ (i.e., a static profile).[1]

The momentum flux (kg m$^{-1}$ s$^{-2}$) at the surface, in turn, is given by

$$\rho_a \nu_t \left(\frac{\partial \mathbf{u}_h^\star}{\partial z^\star}\right)_{z^\star=0} = \rho_a C_D u_h^\star \mathbf{u}_h^\star, \tag{5}$$

where $C_D$ is the so-called (nondimensional) drag coefficient. It can be rewritten in its nondimensional form as

$$\left(\frac{\partial \mathbf{u}_h}{\partial z}\right)_{z=0} = \gamma^{-1} u_h \mathbf{u}_h, \tag{6}$$

with

$$\gamma = \frac{\nu_t}{\Omega H^2 C_D} = \frac{\mathrm{Ek}}{C_D}. \tag{7}$$

The nonlinear relation (6) corresponds to the bottom boundary condition for the velocity in this model. Note that the $\gamma \to 0$ limit traduces a no-slip surface, whereas $\gamma \to \infty$ corresponds to a stress-free surface; the limit $\gamma \to 0$ thus yields the no-slip bottom condition of the original ODD model. The outer radial boundary is no slip and the upper surface $z = 1$ is impermeable but stress free, as in the original setup. A remarkable feature of this configuration is that the bottom mechanical and thermal boundary conditions used in the ODD model can be retrieved by simply setting $\alpha_T = 0$, $\beta_T = 0$, and $\gamma = 0$.

The nondimensional parameters (1) remain unchanged, except that because of the change in the unit of temperature ($\beta H$ in ODD vs $\alpha_T T_s^\star$ in DOE$_1$), the Rayleigh number is now defined as

$$\mathrm{Ra}' = \alpha g \alpha_T T_s^\star H^3 / \nu_t \kappa_t. \tag{8}$$

The whole system is thus controlled by six nondimensional parameters: the three parameters Ek, Pr, and Ra′ which enter the governing equations and the three parameters $\alpha_T$, $\beta_T$, and $\gamma$ which affect the boundary conditions.

### c. *The DOE$_2$ model*

We now introduce a third model, denoted as DOE$_2$, which incorporates a simplified model of the radiative cooling effect. In this setup, the nondimensional equation for heat, using $\alpha_T T_s^\star$ as a unit of temperature, becomes

$$\frac{DT}{Dt} = \mathrm{EkPr}^{-1}\nabla^2 T - \frac{S^\star}{\Omega \alpha_T T_s}, \tag{9}$$

where the last term corresponds to a sink term $S^\star$ being a uniform cooling rate (K s$^{-1}$). The integral of (9) over the domain in the stationary regime yields $S^\star = \alpha_T T_s \kappa_t / H^2$, and (9) can then be rewritten as

$$\frac{DT}{Dt} = \mathrm{EkPr}^{-1}\nabla^2 T - \mathrm{EkPr}^{-1}. \tag{10}$$

The nonhomogeneous additional term accounts for the radiation out of the domain of the energy received from the ocean through surface fluxes. The bottom boundary conditions are the same as in the DOE$_1$ model. The heat fluxes at the upper surface and at the external surface are set to 0. In this configuration, the Rayleigh number (8) thus controls the heat flux at the lower surface which in turn controls the cooling rate $S^\star$. The temperature state at rest $T_{\mathrm{ref}}$ stems from (10) and satisfies the boundary conditions. It takes the form:

$$T_{\mathrm{ref}} = z^2/2 - z. \tag{11}$$

The profile of temperature at rest is no longer linear but is now a quadratic one. The parameter $\beta$ involved in the original model is thus no longer relevant in this model.

## 3. Investigation of the eye formation

To investigate the eye formation, it is convenient to reformulate the Navier–Stokes (1a) and (1b) in the form of two scalar equations. The azimuthal component of (1a) becomes an evolution equation for the specific angular momentum in the rotating frame $\Gamma = r u_\phi$:

$$\frac{D\Gamma}{Dt} = -2 r u_r + \mathrm{Ek}\nabla_\star^2(\Gamma), \tag{12a}$$

$$\text{where} \quad \nabla_\star^2 = r\frac{\partial}{\partial r}\left(\frac{1}{r}\frac{\partial}{\partial r}\right) + \frac{\partial^2}{\partial z^2} \tag{12b}$$

is the Stokes operator. Whereas the curl of the poloidal components yields an evolution equation for the azimuthal vorticity, $\omega_\phi = (\nabla \times \mathbf{u}_p) \cdot \mathbf{e}_\phi$:

[1] Some simulations were also performed using a vanishing heat flux at the external boundary without any qualitative changes in the solution.

$$\frac{D}{Dt}\left(\frac{\omega_\phi}{r}\right) = \frac{\partial}{\partial z}\left(\frac{\Gamma^2}{r^4}\right) + \frac{2}{r}\frac{\partial u_\phi}{\partial z} - \mathrm{RaEk}^2\mathrm{Pr}^{-1}\frac{1}{r}\frac{\partial T}{\partial r} + \frac{\mathrm{Ek}}{r^2}\nabla_\star^2(r\omega_\phi)\cdot \tag{13}$$

These equations are formally equivalent to (2.2)–(2.4) in Oruba et al. (2017). The terms on the right-hand side of (13) correspond to $(\nabla \times \mathbf{F}) \cdot \mathbf{e}_\phi/r$, where $\mathbf{F}$, respectively, stands for part of inertia, buoyancy, Coriolis, and viscosity in (1a). Note that (13) can be rewritten in terms of the streamfunction $\psi$, defined as $\mathbf{u}_p = \nabla \times [(\psi/r)\mathbf{e}_\phi]$ and related to the azimuthal vorticity by $r\omega_\phi = -\nabla_\star^2\psi$.

### a. Numerical simulations and parameter range

Equations (12), (13), and (1c) governing the $\mathrm{DOE}_1$ model, as well as (12), (13), and (10) governing the $\mathrm{DOE}_2$ model, are solved numerically subject to the boundary conditions described in section 2. The simulations, using second-order differences in space and implicit second-order backward differentiation in time, are run until a steady state is reached; the transient regime is thus beyond the scope of this study which focuses on stationary flows. The spatial grid is of size $1000 \times 500$, and the aspect ratio is set to $\varepsilon = 0.1$, a value relevant to real tropical cyclones, with a typical height of some 10 km and a typical radius on the order of 100 km. The turbulent Ekman number Ek is varied between 0.1 and 0.24, in a sensible range for TCs (see the discussion in Oruba et al. 2018), whereas the Prandtl number (Pr) is varied between 0.06 and 1.

The relevant values for the parameters $\alpha_T$, $\beta_T$, and $\gamma$ can be estimated through geophysical considerations. Using the estimate $\kappa_t \simeq 100\ \mathrm{m^2\ s^{-1}}$ for the eddy diffusivity of heat $\kappa_t$ (e.g., Zhang and Drennan 2012) yields $k_a = \kappa_t \rho_a c_p \simeq 10^5\ \mathrm{W\ K^{-1}\ m^{-1}}$. The $\alpha_T$ coefficient is thus on the order of 0.1. Setting $U_g^\star \simeq 1\,\mathrm{m\,s^{-1}}$ (e.g., Godfrey and Beljaars 1991) and $H \simeq 10^4$ m provides $\beta_T \simeq 0.5$. Finally, the $\gamma$ coefficient is estimated to $\gamma \simeq 1.5$ using $C_D = 10^{-3}$ and $\nu_t \simeq 10\ \mathrm{m^2\ s^{-1}}$ (see Chai and Lin 2003; Holton and Hakim 2013). The range explored in our numerical simulations extends from 0.01 to 0.2 for $\alpha_T$, from 0.01 to 1 for $\beta_T$, and from 0.01 to 2 for $\gamma$; beyond these values, nonlinearities become so dominant that only time-varying solutions could be obtained.

### b. Mechanism for eye formation

Figure 1 corresponds to a numerical simulation performed using the ODD model with Ek = 0.1, Pr = 0.1, and Ra = 20 000. Figure 1a highlights the qualitative behavior of the solution: The wind field exhibits a strong cyclonic component driven by the Coriolis force [see (12a)]. Figure 1b shows the azimuthal vorticity of the flow divided by radius $\omega_\phi/r$ and the streamlines associated with the poloidal flow, in the region near the axis. Remember that the height of the domain intends to model the tropical troposphere (some 10 km in height), and Fig. 1b thus extends some 25 km away from the TC center. The streamlines exhibit a main vortex and a countervortex near the axis: This region of reversed flow close to the axis corresponds to the eye. As expected, the azimuthal vorticity field is negative in the bottom boundary layer, and it is also negative in the eyewall.

It is now useful to investigate the effect of the so-called vortex tilting term, i.e., the first term on the right-hand side of (13) on the azimuthal vorticity production. In fact, neglecting viscous effects, buoyancy, and the Coriolis term, close to the axis (see Oruba et al. 2017), the vortex tilting term can be shown to have no net effect. Equation (13) then becomes

$$\mathbf{u}\cdot\nabla\left(\frac{\omega_\phi}{r}\right) = \frac{\partial}{\partial z}\left(\frac{\Gamma^2}{r^4}\right), \tag{14a}$$

because the flow is divergence free, this can be rewritten in the form:

$$\nabla\cdot\left(\frac{\omega_\phi}{r}\mathbf{u}\right) = \frac{\partial}{\partial z}\left(\frac{\Gamma^2}{r^4}\right). \tag{14b}$$

Now considering a flux tube $\mathcal{F}$, bounded by two streamlines and by a fixed radius $r_e$ in the $(r, z)$ plane (see Fig. 2), integrating (14b) over this tube, we get

$$\int_{\partial\mathcal{F}} \frac{\omega_\phi}{r}\mathbf{u}\cdot\mathrm{d}\mathbf{n} = \int\int_{\mathcal{F}} \frac{\partial}{\partial z}\left(\frac{\Gamma^2}{r^4}\right) dS. \tag{14c}$$

Using the Fubini equality, the right-hand side involves an integral in $z$ at fixed $r$ of $(\partial/\partial z)(\Gamma^2/r^4)$. Because $\Gamma$ is constant on each bounding streamline, this integral vanishes for each value of $r$ and so does the right-hand side of (14c). This shows that the vortex tilting term (involving axial gradients in $\Gamma$, in red in Fig. 1c) has no net contribution: The rise and subsequent fall in $\omega_\phi/r$ caused by this term exactly cancel.

Figure 1c presents (black dotted line) the value of $\omega_\phi/r$ along a streamline passing through the eyewall (white thick line in Fig. 1b) as a function of a parametric coordinate along this streamline. This curvilinear coordinate is defined as $dz/d\tau|_{\psi=\mathrm{cst}} = u_z$, with $\tau = 0$ defined as the location where $\omega_\phi/r$ reaches a maximum. This location is indicated with a white dot in Fig. 1b. Figure 1c also represents the contribution of the various terms in (13) along this streamline. The only nonnegligible term in addition to the balance depicted in (14a) is the viscous term. Viscous effects yield a small offset in the vertical alignment of the two minima of $\omega_\phi/r$, indicated by white squares in Fig. 1b.

The mechanism proposed by Oruba et al. (2017) builds on the observations described above. In the ODD model, the eye results from the building of negative azimuthal vorticity in the bottom boundary layer which is nonlinearly advected toward the eyewall where it diffuses inside the eye. This mechanism requires a sufficiently vigorous flow so that it can lift the azimuthal vorticity out of the boundary layer and into the eyewall before it spreads through cross-stream diffusion. For a more complete description, see Oruba et al. (2017, 2018).

To test the applicability of this mechanism to more geophysically realistic forcing, we performed a similar analysis on stationary flows obtained from the new models $\mathrm{DOE}_1$ and $\mathrm{DOE}_2$ (as described in section 2). Figure 3 corresponds to a flow obtained using the $\mathrm{DOE}_1$ model, with Ek = 0.1, Pr = 0.1, Ra′ = 15 000, $\alpha_T = 0.2$, $\beta_T = 0.5$, and $\gamma = 0.7$. The comparison of Figs. 1 and 3 reveals that despite the modification of the boundary conditions, the picture remains unchanged. The force balances in (13) are very similar. Figure 4

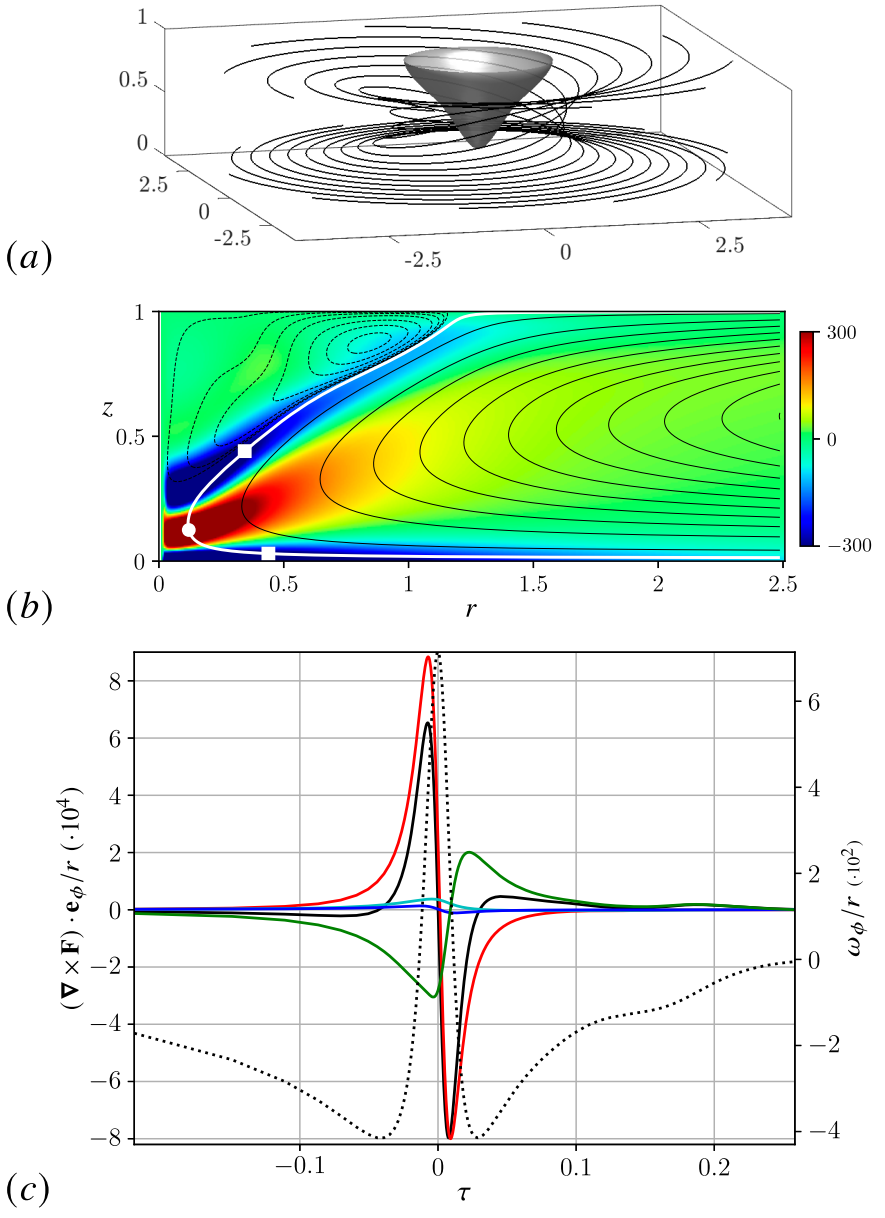


FIG. 1. The ODD model, Ek = 0.1, Pr = 0.1, and Ra = 20 000. (a) Three-dimensional view of the streamlines (black) and the eyewall (gray surface) defined as the iso-surface $\psi = 0$ which separates the main vortex from the countervortex in the eye. (b) The $\omega_\phi/r$ function of $r$ and $z$ near the axis [color code from −300 (blue) to 300 (red)] and streamlines; (c) $(\nabla \times \mathbf{F}) \cdot \mathbf{e}_\phi/r$ following the thick white streamline on (b) inertia (black), axial gradients in Γ (red), Coriolis (dark blue), buoyancy (cyan), and diffusion (green) as a function of $\tau$, a parametric coordinate along the streamline. Dotted black line: $\omega_\phi/r$ along the streamline.

corresponds to a solution obtained using the $DOE_2$ model, with Ek = 0.1, Pr = 0.1, Ra′ = 15 000, $\alpha_T = 0.1$, $\beta_T = 0.5$, and $\gamma = 1$. Again, the implementation of radiative cooling did not modify the general picture.

### c. *Velocity and temperature fields*

It is worth noting that the shape of the eye is, however, affected by the change in boundary conditions. Indeed, in most simulations performed using the ODD model, the eye does not reach the bottom surface (see Figs. 1a,b), whereas in most flows obtained with the $DOE_1$ and $DOE_2$ models, the eye extends to the bottom surface (e.g., Figs. 3a,b and 4a,b). This is also visible in Fig. 5, which shows some additional examples of poloidal flows obtained with these DOE models. The eye is thus more realistic with geophysically relevant boundary conditions. The coefficients $\alpha_T$, $\beta_T$, and $\gamma$ tend to increase the

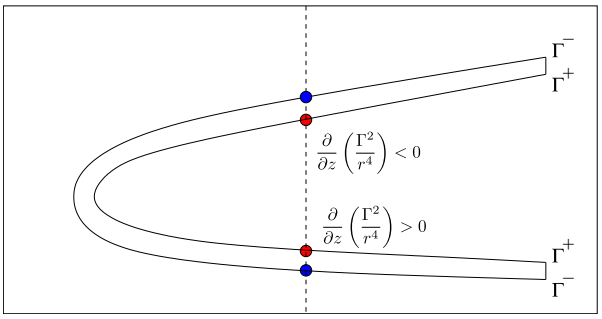


FIG. 2. Sketch for the flux tube $\mathcal{F}$ bounded by two streamlines $\Gamma^+$ and $\Gamma^-$, as introduced in (14c) to estimate the net effect of the vortex tilting term.

strength of the meridional flow in the main vortex. The coefficients $\alpha_T$ and $\beta_T$ increase the efficiency of the thermal driving, whereas the coefficient $\gamma$ reduces the dissipation by viscous drag (while preserving the boundary layer, in the range considered here). This results in a faster circulation and thus more efficient advection of the azimuthal vorticity stripped from the boundary layer. We refer to Oruba et al. (2018) for a discussion of the necessity of this rapid meridional transport in shaping the eye and determining the eye size.

It is also interesting to stress that the slope of the eyewall (varying here from 35° to 45°, from the horizontal) lies in the range observed in real tropical cyclones (e.g., Hazelton and Hart 2013; Stern et al. 2014). Multiple eyes, reminiscent of a double eyewall, were also observed for some ranges of parameters; such structures deserve further investigation and are out of the scope of this paper (see multiple vortices in Figs. 5b,d). This structure may be related to the eyewall replacement in real tropical cyclones.

Figures 6a–c and 6f show the velocity and temperature perturbation fields corresponding to the case shown in Fig. 4 in the first half of the domain. These fields are consistent with the structure of the flow in numerically simulated TCs as well as in real TCs. This figure can, for example, be compared to Figs. 5a–e in Rotunno and Emanuel (1987) or to Figs. 1a–d in Wang and Xu (2010) obtained with the tropical cyclone model, version 4 (TCM4). Besides, the contours associated with the absolute angular momentum, expressed in its nondimensional form as

$$M = \Gamma + r^2, \tag{15}$$

are shown in Fig. 6e. The comparison with streamlines, in Fig. 6d, highlights the alignment of iso-contours of $\psi$ and $M$ except for diffusive effects.

The radial inner flow in the bottom boundary layer is related to the maximum tangential field through the eddy viscosity. Introducing the radial velocity near the surface ($z = 0$) at the radius of maximum wind as $\mathcal{V}$ and the maximum tangential wind speed as $\mathcal{V}_{\max}$, the atmospheric boundary layer provides

$$\mathcal{V} \sim \gamma^{1/2}\mathcal{V}_{\max}. \tag{16}$$

This expression is indeed well verified in the numerical solutions, as highlighted by Fig. 7. The dispersion of numerical data around the best linear fit is quantified in the caption by the mean relative misfit $\chi_{\text{rel}}$:

$$\chi_{\text{rel}} = \sqrt{\frac{1}{n}\sum_{i=1}^{n}\left(\frac{y_i - \hat{y}_i}{y_i}\right)^2}, \tag{17}$$

where $n$ is the number of points, $y_i$ $[i \in (1, n)]$ is the quantity which is fitted, and $\hat{y}_i$ corresponds to the fitted model. In other words, $\chi_{\text{rel}}$ measures the relative ordinate distance between observations and estimations; its use is thus restricted to comparisons of fits for the same quantity $y$.

## 4. Energy budget and scaling laws

We now turn to scaling laws for our models $\text{DOE}_1$ and $\text{DOE}_2$ in order to compare with expressions derived for real tropical cyclones (Emanuel 1997; Bister and Emanuel 1998; Emanuel 2003). These expressions are based on a heat engine model in which the kinetic energy dissipated in the bottom boundary layer is balanced by the external heat input (enthalpy flux through the lower boundary) multiplied by a thermodynamic efficiency. Such a balance yields

$$V_s^2 = \frac{C_K}{C_D}\frac{T_S - T_0}{T_0}(k^\star - k), \tag{18}$$

where $C_K$ and $C_D$ are the dimensionless exchange coefficients for enthalpy and momentum. This formula relates the magnitude of the surface wind $V_s$ to both the temperature difference between the sea surface $T_S$ and the tropopause $T_0$ (also referred to as the "outflow temperature") and the difference between the air enthalpy per unit mass in the boundary layer $k$ and the saturation enthalpy at $T_S$ ($k^\star$). Note that all are here dimensional. This seminal expression, which stems from a thermodynamic equilibrium in the steady state, led the way to numerous formulations for the potential intensity of tropical cyclones (see Emanuel 2018, for a review). Time-dependent theories of TC intensification have also been developed in the last decades (e.g., Wang et al. 2023).

The numerical solutions obtained with our Boussinesq models are steady-state solutions. They thus result from a balance between the kinetic energy frictional dissipation $\mathcal{D}$ and the rate of kinetic energy production $\mathcal{P}$. The latter can be estimated in two different ways: via the external energy input multiplied by a thermodynamic efficiency coefficient (approach widely inspired from the aforementioned heat engine theory) or via the production of kinetic energy by the vertical buoyancy flux.

### a. Kinetic energy dissipation

The dissipation term $\mathcal{D}$ is the power dissipated by the viscous forces in (1a):

$$\mathcal{D} = \text{Ek}\int_\Omega \Delta\mathbf{u}\cdot\mathbf{u}d\mathbf{x}, \tag{19}$$

where $\Omega$ denotes the full three-dimensional domain. Assuming that the dissipation occurs mainly in the boundary layer, it can be approximated as

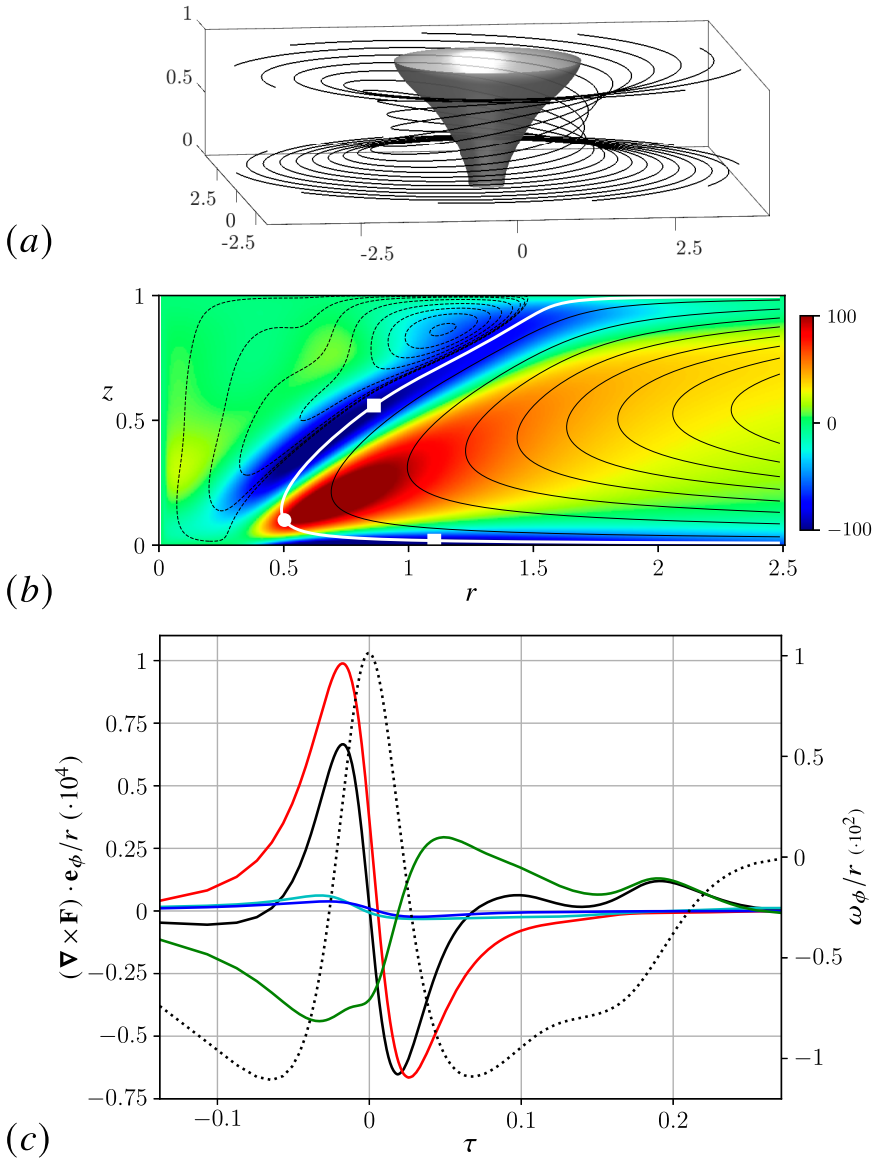


FIG. 3. As in Fig. 1, but using the $\mathrm{DOE}_1$ model, with $\mathrm{Ek} = 0.1$, $\mathrm{Pr} = 0.1$, $\mathrm{Ra}' = 15\,000$, $\alpha_T = 0.2$, $\beta_T = 0.5$, and $\gamma = 0.7$.

$$\mathcal{D} \simeq \mathrm{Ek}\int_\Omega \frac{\partial^2 u}{\partial z^2} u d\mathbf{x} \simeq \mathrm{Ek}\int_{x,y}\left[u\frac{\partial u}{\partial z}\right]_{z=0}^{z=1} - \mathrm{Ek}\int_\Omega \left(\frac{\partial u}{\partial z}\right)^2 d\mathbf{x}, \quad (20)$$

where $\int_{x,y}$ denotes the integral along the horizontal variables only. Following Emanuel (1997), since we assumed that the dissipation in the boundary layer dominates, the second term can be neglected. Injecting the stress-free boundary condition at the top of the domain and the bottom bulk-type condition (6) and assuming that dissipation mainly occurs near the radius of maximum wind yield

$$\mathcal{D} \sim \frac{\mathrm{Ek}}{\gamma}\mathcal{V}^3, \quad (21)$$

which can be rewritten as

$$\mathcal{D} \sim C_D \mathcal{V}^3. \quad (22)$$

This expression is equivalent to formula (5) in Emanuel (2003). We tested this expression on the 79 numerical solutions in our database. The result is represented in Fig. 8. The numerical data points agree with the scaling provided by (22), with moderate deviation as measured by the $\chi_{\mathrm{rel}}$ coefficients (see figure caption). The factor in the right-hand side of (22) depends on the model (either $\mathrm{DOE}_1$ or $\mathrm{DOE}_2$), and both datasets are distinguished in this figure.

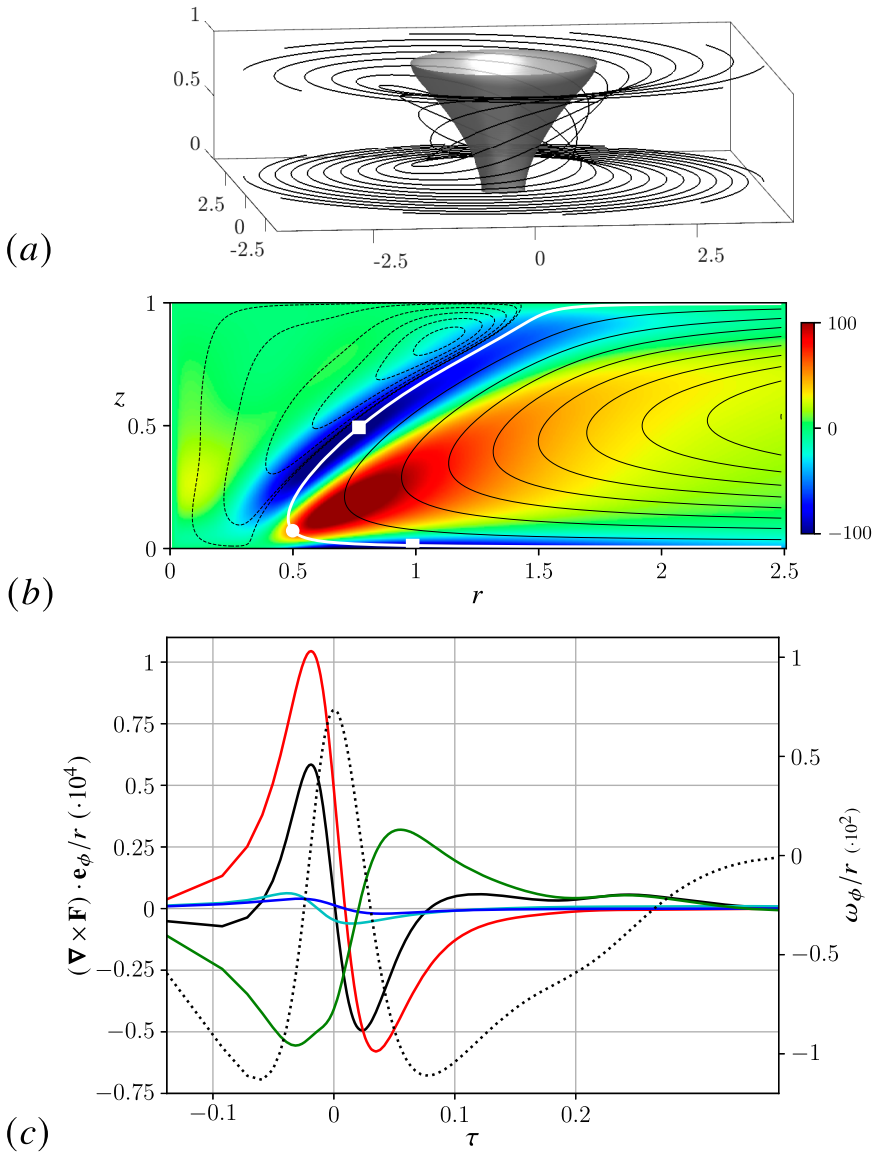


FIG. 4. As in Fig. 1, but using the $DOE_2$ model, with Ek = 0.1, Pr = 0.1, Ra′ = 15 000, $\alpha_T = 0.1$, $\beta_T = 0.5$, and $\gamma = 1$.

### b. *Heat engine theory*

Following a heat engine model, the rate of kinetic energy production, which balances the dissipation, can first be estimated as the external energy input, multiplied by a thermodynamic efficiency coefficient, here denoted as $\varepsilon_c$. In our Boussinesq model, we can use $\alpha \Delta T^\star$ as an estimate of $\varepsilon_c$, with $\Delta T^\star$ being the difference in temperature between the lower and upper boundaries. Using (22) in its dimensional form, the balance between dissipation and production takes the form:

$$\rho C_D \mathcal{V}^{\star 3} \sim \varepsilon_c (F_h^\star - F_{h,0}^\star), \tag{23}$$

where $F_h^\star$ is the surface sensible heat flux and $F_{h,0}^\star$ is its static limit ($\mathcal{V}^\star = 0$). This last term ensures that both sides of (23) vanish when the numerically resolved wind tends to 0. Using the bulk formula (2), we get the nondimensional expression:

$$\mathcal{V}^3 \sim \mathrm{Ra}' \frac{\mathrm{Ek}^2}{\mathrm{Pr}^2} \alpha_T \gamma \frac{c_p \Delta T^\star}{gH} \left[ -\sqrt{1 + \beta_T \mathcal{V}^2} (T - T_s) + (T - T_s)_0 \right]. \tag{24}$$

The value of $(T - T_s)_0$ (i.e., the difference between surface air temperature and the sea surface temperature at rest) can be analytically estimated as $T|_0 = 0$ and $T_s = \alpha_T^{-1}$ for both $DOE_1$ and $DOE_2$ models. We can thus express $(T - T_s)_0 = -\alpha_T^{-1}$. For simplicity (and to guarantee the positivity of $\mathcal{V}$), we thus set $(T - T_s) = (T - T_s)_0 = -\alpha_T^{-1}$. We get

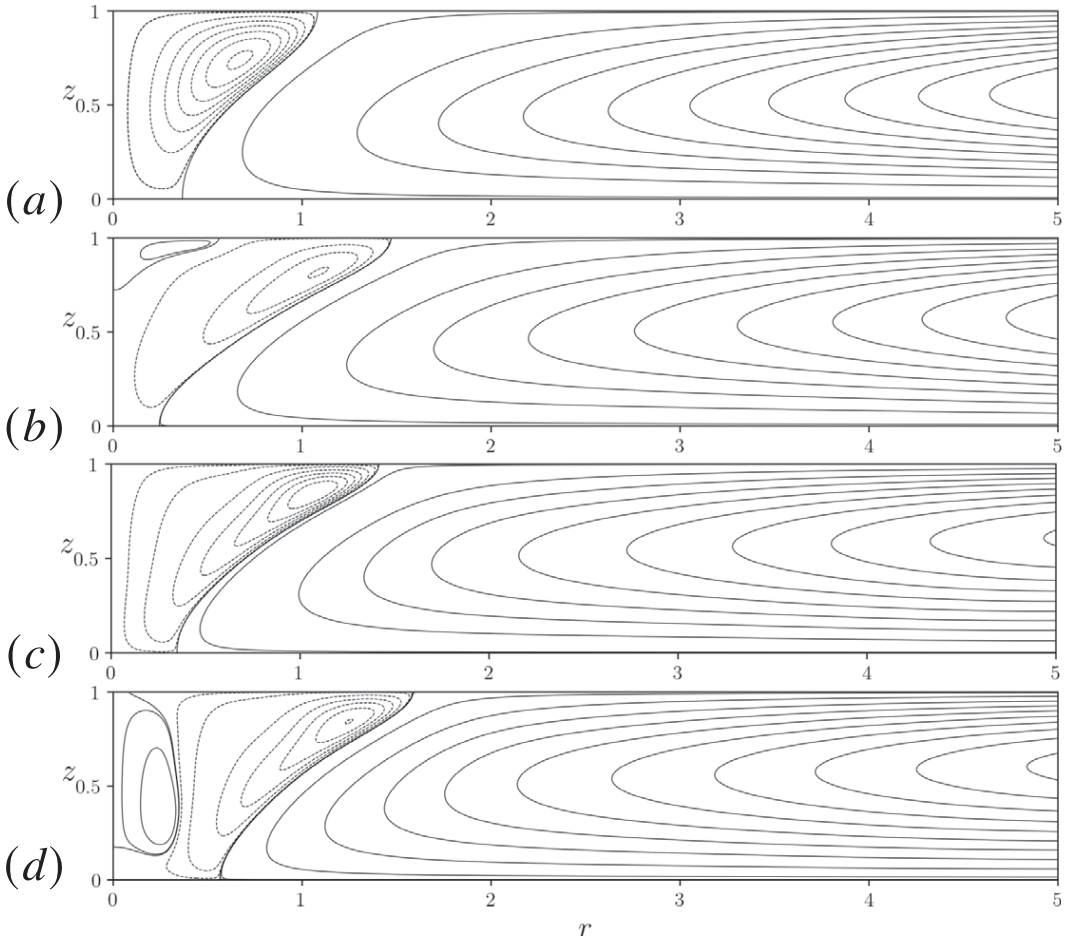


FIG. 5. Streamlines of the poloidal flow obtained with Ek = 0.1 and Pr = 0.1 using the $DOE_1$ model with (a) $Ra' = 2000$, $\alpha_T = 0.05$, $\beta_T = 0.05$, and $\gamma = 0.1$ and (b) $Ra' = 1700$, $\alpha_T = 0.05$, $\beta_T = 0.5$, and $\gamma = 0.5$ and the $DOE_2$ model with (c) $Ra' = 15\,000$, $\alpha_T = 0.1$, $\beta_T = 0.8$, and $\gamma = 0.8$ and (d) $Ra' = 15\,000$, $\alpha_T = 0.1$, $\beta_T = 0.5$, and $\gamma = 2$. Solid lines correspond to clockwise poloidal motion, i.e., $\psi > 0$, and dashed lines correspond to counterclockwise poloidal motion, i.e., $\psi < 0$.

$$\mathcal{V}^3 \sim \chi\left[\sqrt{1+\beta_T\mathcal{V}^2}-1\right], \tag{25}$$

where $\chi$ is defined as

$$\chi = \mathrm{Ra}'\frac{\mathrm{Ek}^2}{\mathrm{Pr}^2}\gamma\frac{c_p\Delta T^\star}{gH}. \tag{26}$$

Note that if $\mathcal{V}$ is redimensionalized ($\Omega H$), and if the definition of the control parameters is inserted in (25), the $\Omega$ factor drops out, as expected in an energy budget.

The $\chi$ coefficient involves both controlling parameters of our Boussinesq equations and a coefficient $c_p\Delta T^\star/(gH)$ which cannot be related to controlling parameters in the Boussinesq formalism. This is due to the simplifying assumptions of the Boussinesq formalism. If the fluid were compressible, this coefficient would be approximately unity if the interior temperature gradient is nearly adiabatic (e.g., Curry and Webster 1998). The Boussinesq formalism can be interpreted as describing a weak perturbation around a nearly adiabatic profile (e.g., Pons and Le Quéré 2005). We therefore set $c_p\Delta T^\star/(gH)$ to unity in following. The result is presented in Fig. 9: As previously mentioned, we note that expression (25) appears well verified by our numerical simulations.

To put further (25) to the test, we now denote the velocity predicted by the heat engine theory, obeying (25), as $\mathcal{V}_{\mathrm{HE}}$ and reformulate (25) as

$$\beta_T^{1/2}\mathcal{V}_{\mathrm{HE}} = f^{-1}(\beta_T^{3/2}\chi), \tag{27}$$

where $f(X) \equiv X^3[(1+X^2)^{1/2}-1]^{-1}$. The $f^{-1}$ function is drawn in Fig. 10. Figure 11 shows the velocity $\mathcal{V}$, as measured in our numerical simulations, as a function of the corresponding value $\mathcal{V}_{\mathrm{HE}}$ predicted by (27). This figure confirms the success of the approach based on a heat engine theory, despite the necessary simplifying assumptions when applied to the Boussinesq formalism.

### c. *Buoyancy force estimates*

Because the standard thermodynamic efficiency approach is complicated by the Boussinesq formalism, we also include a

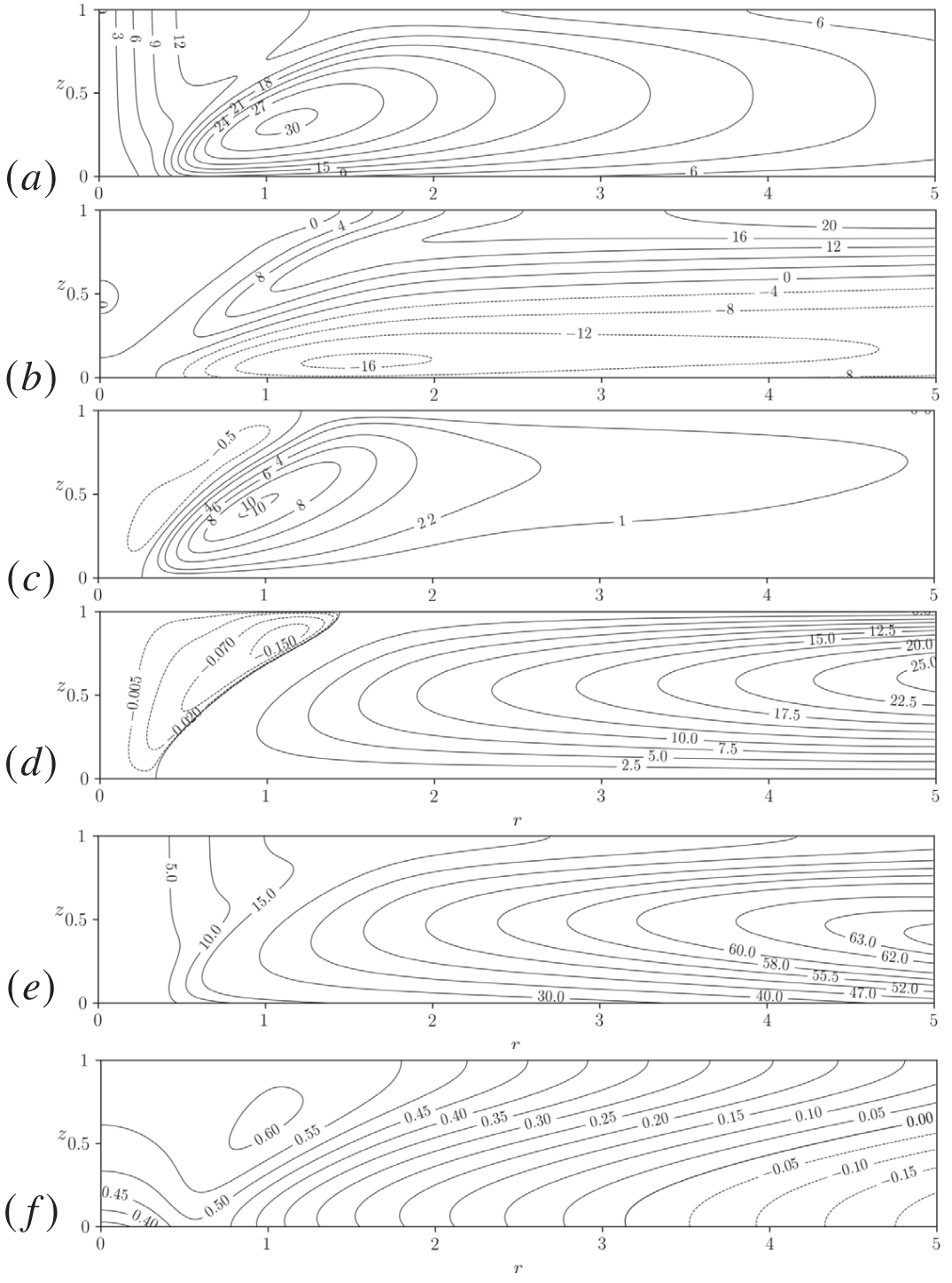


FIG. 6. Structure of the steady-state solution obtained using the model $DOE_2$ with Ek = 0.1, Pr = 0.1, Ra′ = 15 000, $\alpha_T = 0.1$, $\beta_T = 0.5$, and $\gamma = 1$: (a) tangential, (b) radial, (c) vertical velocity, (d) streamfunction, (e) absolute angular momentum, and (f) temperature perturbation fields.

second derivation based on a direct estimate of the power injected in the fluid by buoyancy. We thus estimate the rate of kinetic energy production $\mathcal{P}$ as the power injected by buoyancy forces in (1a):

$$\mathcal{P} = \mathrm{Ra}'\mathrm{Ek}^2\mathrm{Pr}^{-1}\int_\Omega T u_z d\mathbf{x}. \tag{28}$$

Following Emanuel (1997), we assume that the largest contribution to the integrals stems from the flow around the radius

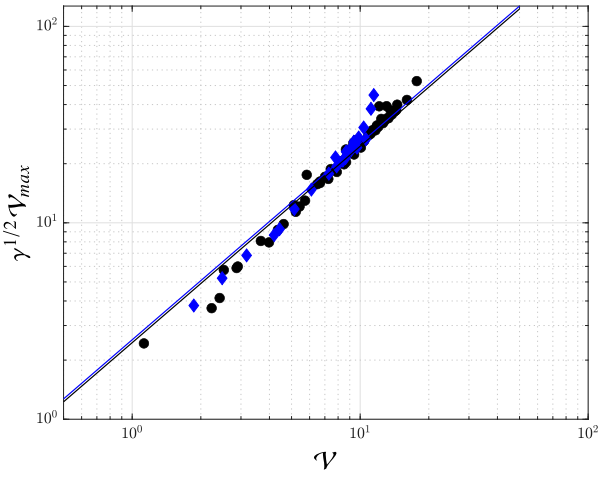


FIG. 7. Validation of (16) against the database. Black and blue colors designate $DOE_1$ and $DOE_2$ models, respectively ($\chi_{rel_1} = 0.13$ and $\chi_{rel_2} = 0.14$).

of maximum wind. Assuming that the vertical $u_z$ in (28) scales as $\mathcal{V}$ (defined in section 3c) and that the temperature $T$ is order unity, $\mathcal{P}$ is expected to vary as

$$\mathcal{P} \sim \mathrm{Ra}'\mathrm{Ek}^2\mathrm{Pr}^{-1}\mathcal{V}. \tag{29}$$

This expression was successfully tested against our database (Fig. 12). The balance of (29) and (22) finally provides

$$\mathcal{V}^2 \sim \mathrm{Ra}'\frac{\mathrm{Ek}}{\mathrm{Pr}}\gamma. \tag{30}$$

This formula relates the velocity $\mathcal{V}$ to the control parameters Ek, Pr, Ra′, and $\gamma$. Again, as was the case in (25), if $\mathcal{V}$ is redimensionalized, $\Omega$ does not enter the resulting expression.

The scaling law (30) is tested against our database in Fig. 13 providing the relative misfits with respect to a linear

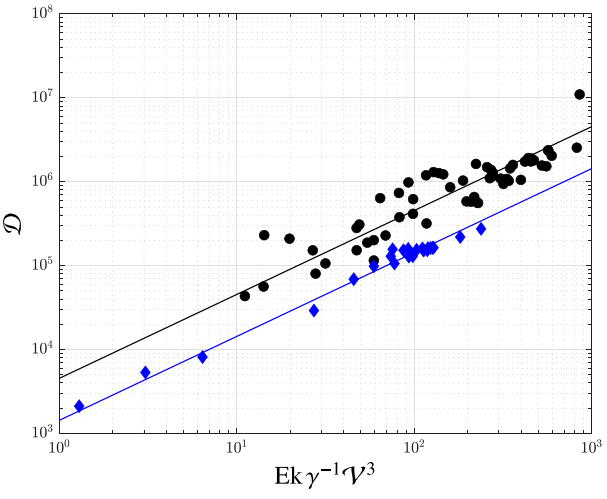


FIG. 8. Validation of (22) expressing the dissipation $\mathcal{D}$ as a function of the combination $\mathrm{Ek}\gamma^{-1}\mathcal{V}^3$ in the $DOE_1$ (black) and $DOE_2$ (blue) models ($\chi_{rel_1} = 0.45$ and $\chi_{rel_2} = 0.16$).

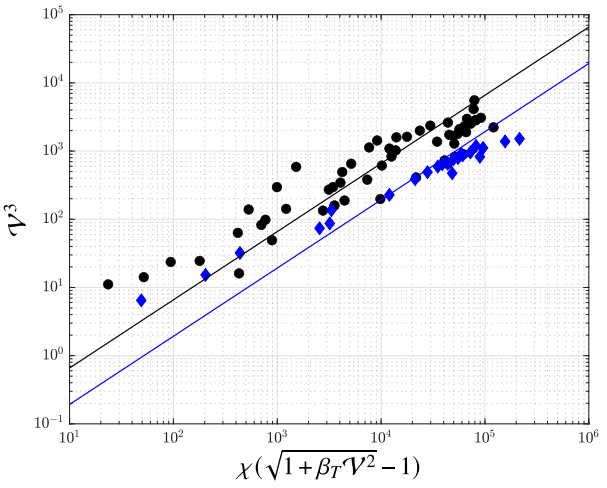


FIG. 9. Representation of the scaling law (25) resulting from a heat engine theory, with the $DOE_1$ (black) and $DOE_2$ (blue) models ($\chi_{rel_1} = 1.27$ and $\chi_{rel_2} = 0.66$).

fit $\chi_{rel_1} = 0.23$ and $\chi_{rel_2} = 0.15$, which confirms the relevance of this analysis to the estimation of the surface wind speed.

Both (25) and (30) involve the product $\mathrm{Ra}'\gamma$ and thus the ratio $C_H/C_D$. Note that $C_H$ is the relevant coefficient in a dry atmosphere and that $C_K$ would appear instead for moist convection. That is consistent with (18). The ratio $C_K/C_D$ has indeed been shown to play an essential role in the intensity of real and simulated TCs (e.g., Bryan 1986).

## 5. Discussion

We considered a simplified dry model for hurricane-like vortices, based on the rotating Rayleigh–Bénard equations. We show that the use of bulk aerodynamic formula to model the heat and momentum fluxes at the bottom boundary, as well as the implementation of a simplified model for radiative

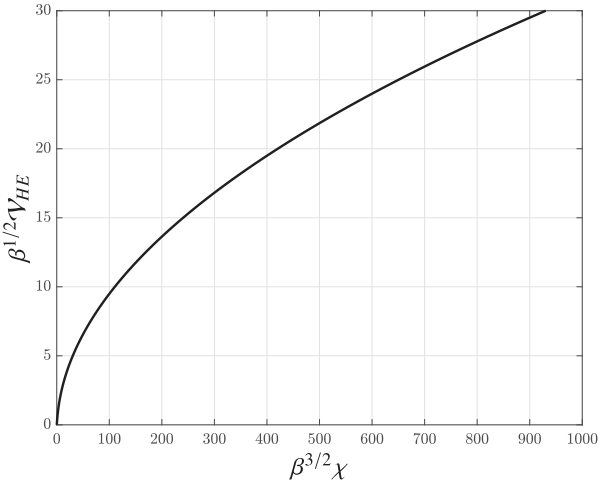


FIG. 10. Representation of the $f^{-1}$ function involved in (27) and relating $\beta_T^{1/2}\mathcal{V}_{\mathrm{HE}}$ to $\beta_T^{3/2}\chi$.

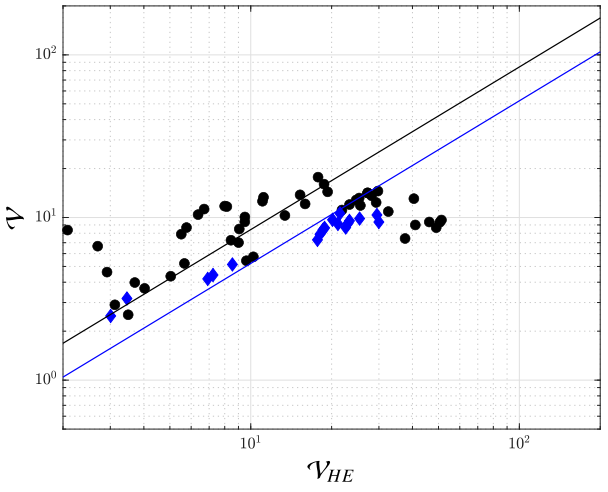


FIG. 11. Velocity $\mathcal{V}$ measured in the $DOE_1$ (black) and $DOE_2$ (blue) models, as a function of the corresponding value $\mathcal{V}_{HE}$, predicted by the heat engine theory ($\chi_{rel_1} = 0.44$ and $\chi_{rel_2} = 0.26$).

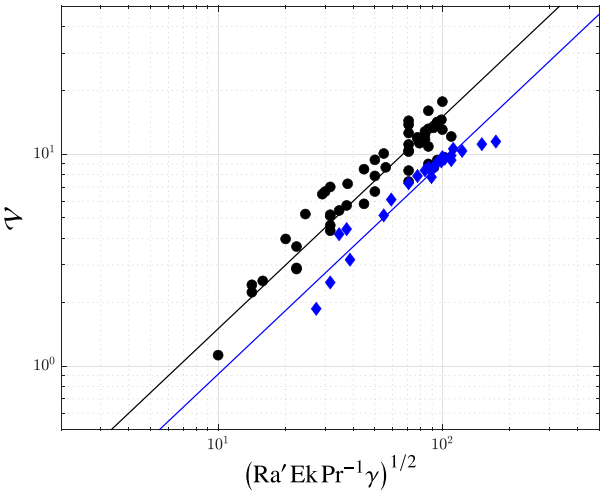


FIG. 13. Representation of the resulting (30) expressing $\mathcal{V}$ vs the combination $(\mathrm{Ra}'\mathrm{EkPr}^{-1}\gamma)^{1/2}$ in the $DOE_1$ (black) and $DOE_2$ (blue) models ($\chi_{rel_1} = 0.23$ and $\chi_{rel_2} = 0.15$).

cooling, yields a more realistic TC-like structure than in Oruba et al. (2017, 2018).

Our work confirms, with more realistic atmospheric boundary conditions (compared to Oruba et al. 2017, 2018), that the negative vorticity in the eyewall of our model is associated with azimuthal vorticity stripping from the bottom boundary layer. The eye then results from cross-stream diffusion. Latent heat release is absent from the model, and the vortex tilting term has no net effect on the azimuthal vorticity. None of these effects are thus involved in the eye formation in this model. The model thus points to the possibility of forming an eye without latent heat release or vortex tilting.

We show that the heat engine approach to determine the maximum sustained wind in a TC from thermodynamic considerations can be extended to the Boussinesq framework by introducing simplifying assumptions on the thermodynamic efficiency. An alternative approach to estimate the energy budget consists in directly trying to estimate the volumetric energy input. In both cases, the maximum wind can be well estimated from the controlling parameters.

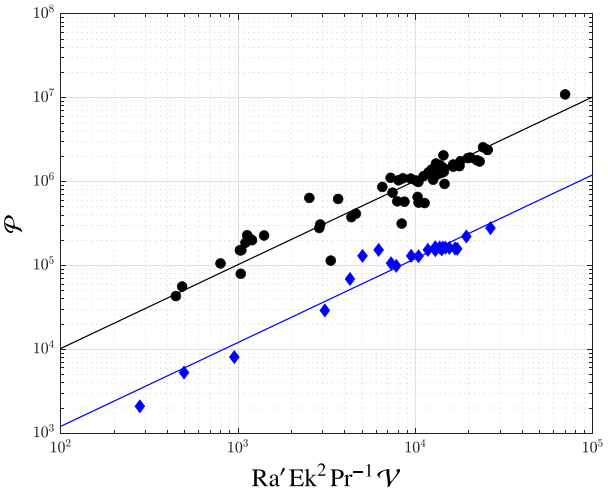


FIG. 12. Validation of (29) resulting from buoyancy force estimates, for the $DOE_1$ (black) and $DOE_2$ (blue) models ($\chi_{rel_1} = 0.47$ and $\chi_{rel_2} = 0.26$).

Two separate issues should be clearly distinguished regarding the eye of tropical cyclones: first, that of the initial formation mechanism of the eye, by which the main poloidal cell does not extend to the axis, and second, that of the subsidence within the eye, once it has formed.

Our mechanism of negative vorticity stripping from the boundary layer could be relevant to the former, i.e., the eye formation. It has to be compared, in real TCs, to other proposed mechanisms such as vortex tilting effects (ineffective in our model). Such inviscid mechanisms rely on the outward slope of angular momentum surfaces (see introduction). Our dry model is interesting in that an eye forms even though the previously proposed mechanisms are ineffective in the considered dry Boussinesq model.

The latter issue of subsidence in the presence of a strong vertical stratification once the eye has formed is, however, far more challenging. The eyes of real TCs are strongly thermally stratified. The absence of latent heat release in our dry model thus has severe dynamical consequences. The cross-stream diffusion, driving the countercirculation in our dry model, would not be enough to counteract the effect of the strong stable stratification. The question of subsidence in a real TC is thus far more complex than in our idealized model, and radiative cooling in the eye is likely to play an essential role. In a real cyclone, cross-stream diffusion would not be enough to maintain an eye on its own and other effects may then become essential. These aspects deserve further studies.

Our mechanism, which again does not include phase change, might have relevance to other atmospheric vortices, such as tornadoes (e.g., Rotunno 2013; Burgess et al. 2002). Further studies with different aspect ratios but also a different

driving will be needed to establish the possible relevance to such structures (tornadoes are not directly driven by surface enthalpy fluxes).

As noted above, our model does not include precipitation and thus the release of latent heat associated with it. A natural development in a future study will be to investigate the effects of water vapor and the release of latent heat via condensation. The effect of water vapor and precipitation could, for example, be incorporated using the formulation of Vallis et al. (2019). Subsidence in a stably stratified eye unquestionably requires other mechanisms than just cross-stream diffusion. Our models exhibit limits which are inherent to the simplifying assumptions on which they rely, but they stress a mechanism (vorticity stripping) which has so far been overlooked.

*Acknowledgments.* This work was initiated in 2018 when Kerry Emanuel was MOPGA visiting professor in Paris, Sorbonne Université. We are most grateful to Prof. R. Rotunno and to three anonymous referees for very useful comments on the submitted version of this work.

*Data availability statement.* The results of numerical simulations presented in this manuscript are available from the authors upon request in the form of a table of controlling parameters and numerical outputs.

## REFERENCES

Atkinson, J. W., P. A. Davidson, and J. E. G. Perry, 2019: Dynamics of a trapped vortex in rotating convection. *Phys. Rev. Fluids*, **4**, 074701, https://doi.org/10.1103/PhysRevFluids.4.074701.

Ballou, S. M., 1892: The eye of the storm. *Amer. Meteor. J.*, **9**, 67–84, 121–127.

Bister, M., and K. A. Emanuel, 1998: Dissipative heating and hurricane intensity. *Meteor. Atmos. Phys.*, **65**, 233–240, https://doi.org/10.1007/BF01030791.

Bryan, G. H., 1986: Effects of surface exchange coefficients and turbulence length scales on the intensity and structure of numerically simulated hurricanes. *J. Atmos. Sci.*, **140**, 1125–1143.

——, and R. Rotunno, 2009: The maximum intensity of tropical cyclones in axisymmetric numerical model simulations. *Mon. Wea. Rev.*, **137**, 1770–1789, https://doi.org/10.1175/2008MWR2709.1.

Burgess, D. W., M. A. Magsig, J. Wurman, D. C. Dowell, and Y. Richardson, 2002: Radar observations of the 3 May 1999 Oklahoma City tornado. *Wea. Forecasting*, **17**, 456–471, https://doi.org/10.1175/1520-0434(2002)017<0456:ROOTMO>2.0.CO;2.

Chai, T., and C.-L. Lin, 2003: Estimation of turbulent viscosity and diffusivity in adjoint recovery of atmospheric boundary layer flow structures. *Multiscale Model. Simul.*, **1**, 196–220, https://doi.org/10.1137/S1540345902411414.

Cronin, T. W., and D. R. Chavas, 2019: Dry and semidry tropical cyclones. *J. Atmos. Sci.*, **76**, 2193–2212, https://doi.org/10.1175/JAS-D-18-0357.1.

Curry, J. A., and P. J. Webster, 1998: *Thermodynamics of Atmospheres and Oceans*. Elsevier, 471 pp.

Dai, Y., M. S. Torn, I. N. Williams, and W. D. Collins, 2023: Longwave radiative effects beyond the initial intensification phase of tropical cyclones. *J. Atmos. Sci.*, **80**, 1829–1845, https://doi.org/10.1175/JAS-D-22-0214.1.

Emanuel, K., 2003: Tropical cyclones. *Annu. Rev. Earth Planet. Sci.*, **31**, 75–104, https://doi.org/10.1146/annurev.earth.31.100901.141259.

——, 2020: The relevance of theory for contemporary research in atmospheres, oceans, and climate. *Amer. Geophys. Union Adv.*, **1**, e2019AV000129, https://doi.org/10.1029/2019AV000129.

Emanuel, K. A., 1997: Some aspects of hurricane inner-core dynamics and energetics. *J. Atmos. Sci.*, **54**, 1014–1026, https://doi.org/10.1175/1520-0469(1997)054<1014:SAOHIC>2.0.CO;2.

——, 2018: 100 years of progress in tropical cyclone research. *A Century of Progress in Atmospheric and Related Sciences: Celebrating the American Meteorological Society Centennial*, *Meteor. Monogr.*, No. 59, Amer. Meteor. Soc., https://doi.org/10.1175/AMSMONOGRAPHS-D-18-0016.1.

Foken, T., 2006: 50 years of the Monin–Obukhov similarity theory. *Bound.-Layer Meteor.*, **119**, 431–447, https://doi.org/10.1007/s10546-006-9048-6.

Godfrey, J. S., and A. C. M. Beljaars, 1991: On the turbulent fluxes of buoyancy, heat and moisture at the air-sea interface at low wind speeds. *J. Geophys. Res.*, **96**, 22 043–22 048, https://doi.org/10.1029/91JC02015.

Hazelton, A. T., and R. E. Hart, 2013: Hurricane eyewall slope as determined from airborne radar reflectivity data: Composites and case studies. *Wea. Forecasting*, **28**, 368–386, https://doi.org/10.1175/WAF-D-12-00037.1.

Holton, J. R., and G. J. Hakim, 2013: *An Introduction to Dynamic Meteorology*. Elsevier, 532 pp.

Kuo, H. L., 1959: Dynamics of convective vortices and eye formation. *The Atmosphere and Sea in Motion*, B. Bolin, Ed., Rockefeller Institute Press, 413–424.

Malkus, J. S., 1958: On the structure and maintenance of the mature hurricane eye. *J. Meteor.*, **15**, 337–349, https://doi.org/10.1175/1520-0469(1958)015<0337:OTSAMO>2.0.CO;2.

Monin, A. S., and A. M. Obukhov, 1954: Basic laws of turbulent mixing in the atmosphere near the ground (in Akan). *Tr. Geofiz. Inst., Akad. Nauk SSSR*, **24**, 163–187.

Mrowiec, A. A., S. T. Garner, and O. M. Paulius, 2011: Axisymmetric hurricane in a dry atmosphere: Theoretical framework and numerical experiments. *J. Atmos. Sci.*, **68**, 1607–1619, https://doi.org/10.1175/2011JAS3639.1.

Muller, C. J., and D. M. Romps, 2018: Acceleration of tropical cyclogenesis by self-aggregation feedbacks. *Proc. Natl. Acad. Sci. USA*, **115**, 2930–2935, https://doi.org/10.1073/pnas.1719967115.

Oruba, L., P. A. Davidson, and E. Dormy, 2017: Eye formation in rotating convection. *J. Fluid Mech.*, **812**, 890–904, https://doi.org/10.1017/jfm.2016.846.

——, ——, and ——, 2018: Formation of eyes in large-scale cyclonic vortices. *Phys. Rev. Fluids*, **3**, 013502, https://doi.org/10.1103/PhysRevFluids.3.013502.

Pearce, R., 2005a: Why must hurricanes have eyes? *Weather*, **60**, 19–24, https://doi.org/10.1256/wea.50.04.

——, 2005b: Comments on "Why must hurricanes have eyes?—Revisited". *Weather*, **60**, 329–330, https://doi.org/10.1256/wea.161.05.

Pearce, R. P., 1998: A study of hurricane dynamics using a two-fluid axisymmetric model. *Meteor. Atmos. Phys.*, **67**, 71–81, https://doi.org/10.1007/BF01277502.

Pons, M., and P. Le Quéré, 2005: An example of entropy balance in natural convection, Part 1: The usual Boussinesq equations. *C. R. Mec.*, **333**, 127–132, https://doi.org/10.1016/j.crme.2004.11.011.

Rotunno, R., 2013: The fluid dynamics of tornadoes. *Annu. Rev. Fluid Mech.*, **45**, 59–84, https://doi.org/10.1146/annurev-fluid-011212-140639.

——, and K. A. Emanuel, 1987: An air–sea interaction theory for tropical cyclones. Part II: Evolutionary study using a nonhydrostatic axisymmetric numerical model. *J. Atmos. Sci.*, **44**, 542–561, https://doi.org/10.1175/1520-0469(1987)044<0542:AAITFT>2.0.CO;2.

Shapiro, L. J., and H. E. Willoughby, 1982: The response of balanced hurricanes to local sources of heat and momentum. *J. Atmos. Sci.*, **39**, 378–394, https://doi.org/10.1175/1520-0469(1982)039<0378:TROBHT>2.0.CO;2.

Smith, R. K., 1980: Tropical cyclone eye dynamics. *J. Atmos. Sci.*, **37**, 1227–1232, https://doi.org/10.1175/1520-0469(1980)037<1227:TCED>2.0.CO;2.

——, 2005: "Why must hurricanes have eyes?"–revisited. *Weather*, **60**, 326–328, https://doi.org/10.1256/wea.34.05.

——, and M. T. Montgomery, 2010: Hurricane boundary-layer theory. *Quart. J. Roy. Meteor. Soc.*, **136**, 1665–1670, https://doi.org/10.1002/qj.679.

Soward, A. M., L. Oruba, and E. Dormy, 2022: Bénard convection in a slowly rotating penny-shaped cylinder subject to constant heat flux boundary conditions. *J. Fluid Mech.*, **951**, A5, https://doi.org/10.1017/jfm.2022.761.

Stern, D. P., J. R. Brisbois, and D. S. Nolan, 2014: An expanded dataset of hurricane eyewall sizes and slopes. *J. Atmos. Sci.*, **71**, 2747–2762, https://doi.org/10.1175/JAS-D-13-0302.1.

Tang, B., and K. A. Emanuel, 2012: Sensitivity of tropical cyclone intensity to ventilation in an axisymmetric model. *J. Atmos. Sci.*, **69**, 2394–2413, https://doi.org/10.1175/JAS-D-11-0232.1.

Vallis, G. K., D. J. Parker, and S. M. Tobias, 2019: A simple system for moist convection: The Rainy–Bénard model. *J. Fluid Mech.*, **862**, 162–199, https://doi.org/10.1017/jfm.2018.954.

Velez-Pardo, M., and T. W. Cronin, 2023: Large-scale circulations and dry tropical cyclones in direct numerical simulations of rotating Rayleigh-Bénard convection. *J. Atmos. Sci.*, **80**, 2221–2237, https://doi.org/10.1175/JAS-D-23-0018.1.

Vigh, J. L., 2010: Formation of the hurricane eye. Ph.D. dissertation, Colorado State University, 538 pp.

Wang, D., and Y. Lin, 2020: Size and structure of dry and moist reversible tropical cyclones. *J. Atmos. Sci.*, **77**, 2091–2114, https://doi.org/10.1175/JAS-D-19-0229.1.

Wang, Y., and J. Xu, 2010: Energy production, frictional dissipation, and maximum intensity of a numerically simulated tropical cyclone. *J. Atmos. Sci.*, **67**, 97–116, https://doi.org/10.1175/2009JAS3143.1.

——, Z.-M. Tan, and J. Xu, 2023: Some refinements to the most recent simple time-dependent theory of tropical cyclone intensification and sensitivity. *J. Atmos. Sci.*, **80**, 321–335, https://doi.org/10.1175/JAS-D-22-0135.1.

Willoughby, H. E., 1979: Forced secondary circulations in hurricanes. *J. Geophys. Res.*, **84**, 3173–3183, https://doi.org/10.1029/JC084iC06p03173.

Wing, A. A., S. J. Camargo, and A. H. Sobel, 2016: Role of radiative–convective feedbacks in spontaneous tropical cyclogenesis in idealized numerical simulations. *J. Atmos. Sci.*, **73**, 2633–2642, https://doi.org/10.1175/JAS-D-15-0380.1.

Zhang, J. A., and W. M. Drennan, 2012: An observational study of vertical eddy diffusivity in the hurricane boundary layer. *J. Atmos. Sci.*, **69**, 3223–3236, https://doi.org/10.1175/JAS-D-11-0348.1.